A uniform metallicity in the outskirts of massive, nearby galaxy clusters

O. Urban[1,2], N. Werner[3,4,5]⋆, S. W. Allen[1,2,6], A. Simionescu[7], A. Mantz[1,2]

[1]*Kavli Institute for Particle Astrophysics and Cosmology, Stanford University, 452 Lomita Mall, Stanford, CA 94305-4085, USA*
[2]*Department of Physics, Stanford University, 382 Via Pueblo Mall, Stanford, CA 94305-4060, USA*
[3]*MTA-Eötvös University Lendület Hot Universe Research Group, Pázmány Péter sétány 1/A, Budapest, 1117, Hungary*
[4]*Department of Theoretical Physics and Astrophysics, Faculty of Science, Masaryk University, Kotlářská 2, Brno, 611 37, Czech Republic*
[5]*School of Science, Hiroshima University, 1-3-1 Kagamiyama, Higashi-Hiroshima 739-8526, Japan*
[6]*SLAC National Accelerator Laboratory, 2575 Sand Hill Road, Menlo Park, CA 94025, USA*
[7]*Institute of Space and Astronautical Science (ISAS), JAXA, 3-1-1 Yoshinodai, Chuo-ku, Sagamihara, Kanagawa, 252-5210, Japan*

March 12, 2018

ABSTRACT

Suzaku measurements of a homogeneous metal distribution of $Z \sim 0.3$ Solar in the outskirts of the nearby Perseus cluster suggest that chemical elements were deposited and mixed into the intergalactic medium before clusters formed, likely over 10 billion years ago. A key prediction of this early enrichment scenario is that the intracluster medium in all massive clusters should be uniformly enriched to a similar level. Here, we confirm this prediction by determining the iron abundances in the outskirts ($r > 0.25r_{200}$) of a sample of ten other nearby galaxy clusters observed with *Suzaku* for which robust measurements based on the Fe-K lines can be made. Across our sample the iron abundances are consistent with a constant value, $Z_{\rm Fe} = 0.316 \pm 0.012$ Solar ($\chi^2 = 28.85$ for 25 degrees of freedom). This is remarkably similar to the measurements for the Perseus cluster of $Z_{\rm Fe} = 0.314 \pm 0.012$ Solar, using the Solar abundance scale of Asplund et al. (2009).

Key words: clusters: intracluster medium – galaxies: X-rays: galaxies: clusters

1 INTRODUCTION

Clusters of galaxies, the most massive objects in the Universe, are continuously growing, both by the steady accretion of matter from their surrounding environment, and by occasional mergers with smaller sub-clusters. The diffuse intergalactic gas accreted by clusters is rapidly shock heated, giving rise to the hot (10^7–10^8 K) X-ray emitting intra-cluster medium (ICM) that pervades clusters. The ICM is in approximate virial equilibrium, with the outer boundary of the virialized region - the virial radius - being approximately equal to $1.3r_{200}$, where within r_{200} the mean enclosed mass density of the cluster is 200 times the critical density of the Universe at the cluster redshift (Lacey & Cole 1993). Galaxy clusters are also unique astrophysical laboratories that allow us to study nucleosynthesis and the chemical enrichment history of the Universe (see Werner et al. 2008). The deep gravitational potential wells of galaxy clusters hold all of the metals ever produced by stars in member galaxies, making them archaeological treasure troves to study the integrated history of star formation (de Plaa et al. 2007; Mernier et al. 2016). The dominant fraction of the metals in clusters currently resides within the hot ICM, which constitutes $\gtrsim 70\%$ of the baryonic mass content for systems above 1.4×10^{14} $M_\odot$ (Giodini

et al. 2009). However, when and how these metals were injected into the intergalactic medium is not well understood.

Most of the line emission from metals in the ICM arises from K- and L-shell transitions of highly ionized elements (see Böhringer & Werner 2010). Because the ICM is in collisional ionization equilibrium and is optically thin, the equivalent widths of the emission lines can be converted directly into elemental abundances. The strongest line emission in the X-ray band is produced by the K-shell transitions of helium-like iron, making it an excellent tracer of chemical enrichment.

It has been known for about 40 years that a significant portion of the hot plasma in the central regions of galaxy clusters (the inner $\sim 0.3r_{200}$) has been enriched by iron produced in stars to about one-third to one-half of the Solar value (Mushotzky et al. 1978, 1981). In the central regions of clusters with strongly peaked ICM density distributions the abundance of iron is also peaked (e.g. De Grandi et al. 2004), but decreases with radius to about one-third Solar (assuming the Solar abundances of Asplund et al. 2009) beyond about $0.2r_{200}$ (Leccardi & Molendi 2008). Due to the low X-ray surface brightness in the outskirts of clusters, metal abundance measurements beyond one-half of the virial radius of clusters remain sparse.

The best measurements of the Fe abundance distribution at large radii were performed using the *Suzaku* Key Project data (1 Ms observation along 8 azimuthal directions) of the Perseus

cluster, which provided 78 data points outside of the cluster core ($r > 0.25r_{200}$). These data revealed a remarkably uniform iron abundance, as a function of radius and azimuth, that is statistically consistent with a constant value of $Z_{Fe} = 0.314 \pm 0.012$ Solar (using the Solar abundance scale of Asplund et al. 2009) out to r_{200} (Werner et al. 2013). Subsequent *Suzaku* observations of the Virgo cluster extended these measurements to elements other than iron indicating an uniform chemical composition throughout the cluster volume (Simionescu et al. 2015). The observed homogeneous distribution suggests that most of the metal enrichment of the ICM occurred before the cluster formed and its entropy distribution became stratified, preventing further efficient mixing. A key prediction of this early enrichment scenario is that the ICM in all massive clusters should be uniformly enriched to a similar level (Werner et al. 2013; Fabjan et al. 2010; Biffi et al. 2017).

In order to test these predictions, we have analysed all archival observations of nearby galaxy clusters observed with *Suzaku* for which data extend to $r \sim r_{200}$ and robust measurements based on the Fe-K lines can be performed at $r > 0.25r_{200}$. (Because the Fe-K complex is by far the strongest line complex in the X-ray spectrum, the word metallicity will in this paper refer to and will be used interchangeably with the Fe abundance.) Our sample spans a redshift range $z = 0.017$–0.183 and a temperature range of about 2.5–9 keV (the corresponding range of virial masses is about 1.4–$14 \times 10^{14} M_\odot$; Arnaud et al. 2005). The selected temperature range permits metallicity measurement using the Fe-K lines, allowing us to largely avoid multi-temperature biases arising from the measurements of the Fe-L complex (Buote 2000).

Sect. 2 describes the data analysis, spectral modeling, and the treatment of the X-ray background. In Sect. 3, we present the results. Finally, in Sect. 4 and 5, we briefly discuss the implications of these results and draw our conclusions.

2 OBSERVATIONS AND DATA ANALYSIS

The details of the *Suzaku* observations for each of the 9 clusters analyzed in this study are shown in Tab. 1. For each cluster we analyzed the data from all available X-Ray Imaging Spectrometers (XIS 0, 1, 2[1], 3).

2.1 Data Reduction

We obtained the initial cleaned event lists using the standard criteria provided by the XIS team[2]. There is a gradual increase in the number of flickering pixels in the XIS detectors with time, which may affect the measurements, if unaccounted for. We used maps provided by the XIS team[3] to remove the flickering pixels from the cluster observations, as well as from the night Earth observations, which were later used to create the non-X-ray background (NXB) data products.

We checked for likely solar wind charge-exchange (SWCX) emission contamination using the WIND Solar Wind Experiment

---

[1] XIS2 was lost to a likely micrometeoroid hit on 2006 November 9, and therefore its data are available only for the observations from before this date.

[2] Arida, M., XIS Data Analysis,
http://heasarc.gsfc.nasa.gov/docs/suzaku/analysis/abc/node9.html

[3] The current maps, as well as the recipe for the removal process, are available at http://www.astro.isas.ac.jp/suzaku/analysis/xis/nxb_new/

Table 1. Details of *Suzaku* observations used in the analysis. The columns show, respectively, the target name, the *Suzaku* observation ID, the date of the observation and the clean exposure time.

Name	Obs. ID	Obs. date	Exposure (ks)
ABELL 262 CENTER	802001010	2007-08-17	10.9
ABELL 262 OFFSET 1†	802079010	2007-08-06	11.0
ABELL 262 OFFSET 2	802080010	2007-08-08	14.6
NCG 669†	804049010	2009-07-05	50.3
A262 NE1	808108010	2014-02-14	8.4
A262 NE2†	808109010	2014-02-15	1.4
A262 NE3†	808110010	2014-02-15	9.8
A262 NE4	808111010	2014-02-16	31.0
A262 E1	808112010	2014-02-06	9.2
A262 E2†	808113010	2014-02-07	5.4
A262 E3	808114010	2014-02-13	10.9
A262 E4†	808115010	2014-02-13	9.8
ABELL 1795†	800012010	2005-12-10	13.1
ABELL 1795 Near North†	800012020	2005-12-10	24.4
ABELL 1795 Far North	800012030	2005-12-11	5.9
ABELL 1795 Near South	800012040	2005-12-11	11.2
ABELL 1795 Far South	800012050	2005-12-12	12.5
A1795_FAR_NORTHEAST†	804082010	2009-06-28	4.7
A1795_FAR_SOUTHWEST	804083010	2009-06-29	8.3
A1795_FAR_WEST	804084010	2009-06-26	8.5
A1795_NEAR_WEST	804085010	2009-06-27	4.1
A1689-OFFSET1	803024010	2008-07-23	9.1
A1689-OFFSET2	803025010	2008-07-24	7.5
A1689-OFFSET3	803026010	2008-07-25	8.9
A1689-OFFSET4†	803027010	2008-07-26	6.2
ABELL 1689 (OFFSET)†	808089010	2013-06-27	17.5
ABELL 1689 (OFFSET)	808089020	2013-06-30	6.4
ABELL 1689 (OFFSET)	808089030	2013-12-31	53.2
ABELL 1689 (OFFSET)	808089040	2014-01-13	7.1
HYDRA A-1†	805007010	2010-11-08	6.9
HYDRA A-2	805008010	2010-11-09	6.9
HYDRA A SE	807087010	2012-06-07	5.5
HYDRA A FAR SE	807088010	2012-06-04	5.6
HYDRA A FAR N	807089010	2012-06-05	5.6
HYDRA A SW†	807090010	2012-11-10	39.8
HYDRA A OUT	807091010	2012-06-07	0.3
ABELL 2029†	802060010	2008-01-08	27.6
A2029_1	804024010	2010-01-28	3.5
A2029_2	804024020	2010-01-28	2.6
A2029_3	804024030	2010-01-28	6.3
A2029_4	804024040	2010-01-29	1.9
A2029_5†	804024050	2010-01-30	3.5
A2142	801055010	2007-01-04	12.0
A2142 OFFSET 1	802030010	2007-08-04	7.1
A2142 OFFSET 2	802031010	2007-09-15	57.7
A2142 OFFSET 3	802032010	2007-08-29	7.0
FILAMENT OF GALAXIES	805029010	2010-07-29	19.9
ABELL 2204	801091010	2006-09-17	14.3
A2204_FIELD_1†	805056010	2010-09-01	5.9
A2204_FIELD_2	805057010	2010-08-27	6.9
A2204_FIELD_3	805058010	2010-08-28	6.8
A133_W	805019010	2010-06-07	50.0
A133_N	805020010	2010-06-05	50.2
A133_E†	805021010	2010-06-09	51.6
A133_S†	805022010	2010-06-08	51.1
A133_FIELD_1	808081010	2013-12-19	53.6
A133_FIELD_2	808082010	2013-12-20	50.6
A133_FIELD_3	808083010	2013-12-05	51.9
A133_FIELD_4†	808084010	2013-12-06	52.5
SWIFT J0250.7+4142	709006010	2014-08-03	82.2
AWM7†	801035010	2006-08-07	19.0
AWM7 EAST OFFSET	801036010	2006-08-05	38.5
AWM7 WEST OFFSET†	801037010	2006-08-06	39.8
AWM7 EAST OFFSET	802044010	2008-01-27	85.6
AWM7 SOUTH OFFSET†	802045010	2008-01-29	31.3
AWM7 SOUTH OFFSET†	802045020	2008-02-23	91.2
AWM7 45' EAST	806008010	2011-08-07	36.9
AWM7 27' SOUTH†	806009010	2012-02-18	35.0
AWM7 45' SOUTH	806010010	2012-02-17	34.4
AWM7 NW1	808023010	2014-02-17	14.9
AWM7 NW2†	808024010	2014-02-17	35.3
AWM7 SE1	808025010	2014-02-18	16.8
AWM7 SE2†	808026010	2014-02-19	35.3

† observations influenced by SWCX

Table 2. Central coordinates, redshifts, mean temperatures, and values of r_{200} for the clusters in our sample. The central coordinates are from the MCXC (Piffaretti et al. 2011), except for A 1689, which are from the RASS-BSC (Voges et al. 1999).

	RA (J2000)	dec (J2000)	z	$kT^{\dagger}_{\mathrm{ref}}$ (keV)	$r_{200,\mathrm{ref}}$ (Mpc)
A 262	01h 52m 46.8s	+36° 09' 05"	0.017	2.3	1.52 (Neill et al. 2001)
A 1795	13h 48m 53.0s	+26° 35' 44"	0.063	6.2	1.90 (Bautz et al. 2009)
A 1689	13h 11m 29.5s	−01° 20' 14"	0.183	8.6	2.50 (Umetsu & Broadhurst 2008)
Hydra A	09h 18m 06.5s	−12° 05' 36"	0.054	3.8	1.48 (Sato et al. 2012)
A 2029	15h 10m 55.0s	+05° 43' 14"	0.077	7.9	1.92 (Walker et al. 2012)
A 2204	16h 32m 46.5s	+05° 34' 14"	0.152	6.4	1.84 (Reiprich et al. 2009)
A 2142	15h 58m 20.6s	+27° 13' 37"	0.091	8.5	2.48 (Akamatsu et al. 2011)
A 133	01h 02m 42.1s	−21° 52' 25"	0.057	4.0	1.60 (Morandi & Cui 2014)
AWM 7	02h 54m 29.5s	+41° 34' 18"	0.017	3.7	1.47 (Walker et al. 2014)

$\dagger$Ikebe et al. (2002)

data[4], following the analysis of Fujimoto et al. (2007). In the case of affected pointings, marked in Tab. 1, we only used data above 1.5 keV, where no SWCX emission lines are expected.

We filtered out times of low geomagnetic cut-off rigidity (COR>6 GV). Ray-tracing simulations of spatially uniform extended emission were used to perform vignetting corrections (Ishisaki et al. 2007). For the XIS 1 data obtained after the reported charge injection level increase on 2011 June 1st, we have excluded two adjacent rows on either side of the charge-injected rows. (The standard is to exclude one row on either side.)

2.2 Image analysis

We extracted images from all XIS detectors in the $0.7 - 7.0$ keV energy band, removing ~ 30 arcsec regions around the edges. We extracted instrumental background images in the same energy band from flickering-pixel-subtracted night Earth observations using the tool XISNXBGEN. We subtracted the background images from the cluster images before applying the vignetting correction. The resulting mosaics for each cluster are shown in Figs. A1–A9.

2.3 Point Source Detection

The initial identification of the point sources was carried out using the CIAO tool WAVDETECT. We used a single wavelet radius of 1 arcmin, which is approximately matched to the half-power radius of the X-ray telescopes on *Suzaku*. For each cluster we created a candidate set of point sources assuming a source with a radius of 1 arcmin at each of the positions identified by WAVDETECT. We then calculated X-ray surface brightness profiles centered on the coordinates in Tab. 2, excluding the candidate set of point sources, and fitted an isotropic β-model to the surface brightness profile of each cluster:

$$S_X = S_0 \left[1 + \left(\frac{r}{r_c} \right)^2 \right]^{(-3\beta+0.5)} + S_{X,\mathrm{bkg}}, \qquad (1)$$

where r is the distance from the cluster center and the free parameters are the normalization S_0, the core radius r_c and β. $S_{X,\mathrm{bkg}}$ is the surface brightness of the X-ray background, which is assumed to be constant across the whole area of the cluster. The best-fit parameters for the individual clusters are shown in Tab. 3.

We divided the mosaic images of the individual clusters by the best-fit surface brightness models and used the resulting residual

4 The data are available at: ftp://space.mit.edu/pub/plasma/wind/kp_files/

Table 3. β model parameters for each cluster. See Eqn. 1 for the interpretation of the individual columns. Parameters S_0 and $S_{X,\mathrm{bkg}}$ are in the units of counts/s/pixel^2 and the core radius r_c is in *Suzaku* pixels, where 1 arcmin = 7.2 pixels.

	$S_0 \times 10^5$	r_c	β	$S_{X,\mathrm{bkg}} \times 10^7$
A 262	1.45 ± 0.05	18.3 ± 0.7	0.51 ± 0.01	0.98 ± 0.035
A 1795	7.78 ± 0.26	14.7 ± 0.4	0.70 ± 0.01	0.90 ± 0.04
A 1689	4.40 ± 0.43	10.6 ± 0.8	0.78 ± 0.02	1.18 ± 0.03
Hydra A	3.88 ± 0.23	14.1 ± 0.8	0.67 ± 0.02	1.03 ± 0.06
A 2029	9.52 ± 0.37	14.1 ± 0.5	0.69 ± 0.01	1.37 ± 0.04
A 2204	4.44 ± 0.17	16.5 ± 0.7	0.93 ± 0.03	2.89 ± 0.08
A 2142	4.58 ± 0.11	20.3 ± 0.6	0.70 ± 0.01	8.15 ± 0.05
A 133	0.96 ± 0.07	13.3 ± 0.9	0.73 ± 0.02	0.71 ± 0.04
AWM 7	2.37 ± 0.05	29.4 ± 0.8	0.55 ± 0.01	0.75 ± 0.04

images to identify by eye sources with radii larger than 1 arcmin. In these cases, we manually increased the sizes of the sources in question by the appropriate amount. The resulting updated sets of point sources (including substructures and artifacts that can appear at chip edges), which were excluded from the subsequent spectral analysis, are shown with magenta circles in Figs A1 – A9.

2.4 Spectral Analysis

For each cluster, we extracted spectra from a series of concentric annular regions centered on the respective cluster's centre (see Tab. 2). The width of the annuli was set to be at least 3 arcmin, with each annulus containing at least 3500 cluster counts, allowing us, in principle, to measure the Fe abundance with a relative uncertainty of at most 20%. The resulting annuli are shown in yellow in Figs. A1–A9. Instrumental background spectra were created using Night Earth observations.

We rebinned each spectrum to a minimum of one count per bin, employing the extended C-statistic (Cash 1979; Arnaud 1996) in the fitting. For each spectrum, we constructed an individual response matrix with a resolution of 16 eV, spanning the $0.2-9.5$ keV energy band[5]. We used the task XISSIMARFGEN (version 2010-11-05) to create ancillary response files (assuming uniform emission from a circular region with the radius of 20 arcmin).

We used XSPEC (Arnaud 1996, version 12.9.0) to model the

5 These rebinned matrices require ~ 25 times less disk space compared to the default choice of 2 eV resolution and the full $0.2 - 16.0$ keV *Suzaku* energy band, allowing us to model all the spectra for a given cluster simultaneously and speeding up the analysis, without compromising the accuracy of the results.

spectra. For each cluster we modeled all spectra simultaneously, using the 0.7 − 7.0 keV band for the front illuminated XIS 0, XIS 2 and XIS 3 detectors, and the 0.6 − 7.0 keV band for the back illuminated XIS 1, except for observations with possible SWCX contamination (see Tab. 1), where we used the 1.5 − 7.0 keV energy band. We modeled the ICM emission in each annulus as a single temperature plasma in collisional ionisation equilibrium using the absorbed APEC (ATOMDB 3.0.3) model (Smith et al. 2001).

For a given annulus, we used a single temperature and metallicity. Normalizations were allowed to vary among individual observations, but were tied among the detectors in a single observation; in other words, all spectra from a given observation were members of a single fitting group in xspec. We used the abundance table of Asplund et al. (2009) in the analysis. Galactic absorption was set to the average column along the line of sight inferred from the Leiden/Argentine/Bonn Survey (Kalberla et al. 2005). The uncertainties in all derived parameters were determined using Markov Chain Monte Carlo (MCMC) simulations. After removing the burn in period and thinning each chain, we used the mean and the standard deviation as the value and the uncertainty of each derived parameter, respectively.

2.5   Modeling the X-ray Foreground and Background

At large clustercentric radii, the cosmic X-ray foreground/background (CXFB) makes up a dominant fraction of the total X-ray emission, requiring careful modeling. Our spectral model for the CXFB included four components – an absorbed power law (PL) due to the unresolved point sources (De Luca & Molendi 2004), an absorbed thermal component modeling the Galactic halo emission (GH, Kuntz & Snowden 2000), a potential 0.6 keV foreground component that we will from now on refer to as the hot foreground (HF, Masui et al. 2009; Yoshino et al. 2009), and an unabsorbed thermal component modeling the emission from the local hot bubble (LHB, Sidher et al. 1996).

In order to better constrain the low-temperature CXFB components, we used the X-Ray Background Tool[6], which calculates the average X-ray background spectra from the ROSAT All-Sky Survey diffuse background maps. For each cluster we obtained spectra from six independent circular regions with radii $R = 1.3r_{200}$ evenly surrounding the cluster so that each touches the outer edge of a circle with radius $r = 1.3r_{200}$ centered on the cluster core, as well as two neighbouring background regions. The distance from the cluster core ensures that the spectra are not significantly contaminated by emission from the ICM. This setup, as opposed to using a single annular region, allowed us to assign separate absorptions to each of the six regions, which can potentially significantly influence the modeling at *ROSAT* energies, 0.7 − 2.0 keV.

As stated before, for each cluster we modeled all spectra simultaneously, including the CXFB model. To limit the systematic effects that might potentially influence the fit, we first separately determined the PL parameters, that were kept fixed during the subsequent modeling. To do this, we used the spectra from the outermost annulus in a given cluster in the high energy band, 2.0 − 7.0 keV, where the PL component is dominant at large clustercentric radii. For six of the clusters in our sample, A 133, A 1689, A 1795, A 2029, A 2142, and A 2204, the outermost annulus covers only regions outside r_{200}. In these cases, we assumed no significant cluster

emission to contribute to the spectrum and therefore the high energy fit included only the PL model. For the remaining clusters, A 262, AWM 7 and Hydra A, we accounted for potential cluster emission by including an APEC component in the high energy fit, fixing its temperature to $kT = 2$ keV and keeping the normalizations in the individual observations free. The best-fit PL parameters are shown in the first two columns of Tab. 4.

In the subsequent spectral modeling, the remaining CXFB parameters were kept free and tied among all spectra from a given cluster, with the exception of the metallicity and the redshift of the three thermal components, which were fixed at unity and zero, respectively.

For each cluster, we tied together the ICM temperatures and Fe abundances in the neighboring annuli where required in order to obtain a statistically significant constraint. The final CXFB model parameters for the individual clusters are listed in Tab. 4.

### 2.6   Criteria For Robust Metallicity Measurements

In each cluster we formally obtained profiles of temperature and metallicity out to the outermost radii reached by the observations. However, due to the low surface brightness of the ICM, the measurements at large radii may be significantly influenced by systematic uncertainties, such as potential variations of the CXFB model throughout the cluster. To address our main scientific questions, it is therefore crucial to only use the metallicity measurements which we are confident about. We used the following criteria to identify these measurements:

• We only used the measurements at radii $r > 0.25r_{200}$ to avoid the central metallicity peak observed in most cool-core galaxy clusters. We used a similar radial range in the Perseus cluster (Werner et al. 2013), where metallicity measurements inside 20′ ($r_{200} = 82′$) were discarded.

• We only used annuli with ICM-signal-to-background (ISB) ratios around the Fe-K lines higher than 10%. This is defined as the ratio of the total number of modeled counts received from the ICM to the sum of modeled counts from the CXFB and the instrumental background, in a 1 keV wide energy band centered on the appropriately redshifted Fe-K line (rest energy $E = 6.7$ keV). The top right panels in Figs. A1–A9 show the profiles of the ISB ratios for the individual annuli (in blue), as well as the ratios for the individual observations (in red). The 10% threshold is broadly consistent with the measurements in the outermost regions of the Perseus cluster (Werner et al. 2013; Urban et al. 2014).

• Finally, we only used the annuli where the contamination from the neighbouring regions due to the wings of the broad point spread function (PSF) of the telescopes is small. The half-power diameter (HPD) of the X-ray Telescopes (XRT) on board of *Suzaku* is ∼ 2′, which causes a fraction of the emission from an object to be registered elsewhere on the detector. Addressing this issue is especially important in the cool core clusters at relatively large distances ($z \gtrsim 0.1$), since the emission from the metal-rich X-ray surface brightness peak may bias spectral measurements out to larger radii. To test for this, we used *Chandra* surface brightness profiles with high spatial resolution relative to *Suzaku* (binned to ∼ 4″), which we convolved with a simple Gaussian model for the *Suzaku* point-spread function with a HPD of 2 arcmin. Using this model, for each of our annuli we calculated the fraction of emission that we expected to come from the other annuli, and removed those where it exceeded 10%. Only the two most distant clusters in our sample, A 2204 and A 1689, were affected. For both systems, we re-

---

[6] http://heasarc.gsfc.nasa.gov/cgi-bin/Tools/xraybg/xraybg.pl

Table 4. The CXFB model parameters for the individual clusters. The four CXFB model components we used are the power-law component (PL), the Galactic halo (GH), the hot foreground component (HF) and the Local Hot Bubble (LHB). Subscript n stands for normalization, kT for temperature and ind for index. Normalizations are in units of $\int n_e n_H \, dV \times \frac{10^{-14}}{4\pi[D_A(1+z)]^2} \frac{1}{20^2\pi}$ cm^{-5} arcmin^{-2}.

	PL$_{ind}$	PL$_n\times10^4$	GH$_{kT}$	GH$_n\times10^3$	HF$_{kT}$	HF$_n\times10^4$	LHB$_{kT}$	LHB$_n\times10^4$
A 262	$1.43^{+0.05}_{-0.05}$	$9.38^{+0.67}_{-0.64}$	$0.18^{+0.01}_{-0.01}$	$2.82^{+0.13}_{-0.19}$	$0.94^{+0.04}_{-0.05}$	$2.59^{+0.12}_{-0.22}$	$0.103^{+0.002}_{-0.002}$	$9.01^{+0.18}_{-0.30}$
A 1795	$1.38^{+0.05}_{-0.08}$	$10.07^{+0.84}_{-0.79}$	$0.22^{+0.01}_{-0.01}$	$0.91^{+0.18}_{-0.08}$	N/A	N/A	$0.10^{+0.01}_{-0.01}$	$49.10^{+0.26}_{-0.36}$
A 1689	$1.34^{+0.04}_{-0.03}$	$9.16^{+0.47}_{-0.41}$	$0.18^{+0.01}_{-0.02}$	$2.43^{+0.50}_{-0.40}$	$0.59^{+0.05}_{-0.03}$	$2.11^{+0.64}_{-0.32}$	$0.10^{+0.01}_{-0.01}$	$13.65^{+0.23}_{-0.20}$
Hydra A	$1.39^{+0.07}_{-0.09}$	$8.61^{+1.15}_{-0.90}$	$0.12^{+0.01}_{-0.01}$	$4.45^{+1.40}_{-1.30}$	$0.79^{+0.11}_{-0.16}$	$1.91^{+0.36}_{-0.16}$	$0.10^{+0.01}_{-0.01}$	$9.53^{+1.20}_{-1.20}$
A 2029	$1.25^{+0.07}_{-0.08}$	$7.01^{+0.69}_{-0.63}$	$0.18^{+0.01}_{-0.02}$	$6.18^{+1.15}_{-1.05}$	$0.58^{+0.02}_{-0.01}$	$13.95^{+0.90}_{-1.30}$	$0.10^{+0.01}_{-0.01}$	$13.4^{+0.19}_{-0.37}$
A 2204	$1.49^{+0.10}_{-0.10}$	$12.52^{+1.62}_{-1.47}$	$0.227^{+0.008}_{-0.005}$	$10.63^{+0.45}_{-2.25}$	$0.61^{+0.02}_{-0.02}$	$10.25^{+0.22}_{-0.12}$	$0.13^{+0.06}_{-0.01}$	$17.50^{+1.08}_{-2.00}$
A 2142	$1.37^{+0.06}_{-0.05}$	$9.19^{+0.64}_{-0.61}$	$0.146^{+0.004}_{-0.004}$	$4.88^{+55}_{-0.55}$	$0.64^{+0.06}_{0.02}$	$2.51^{+0.14}_{-0.22}$	$0.09^{+0.01}_{-0.01}$	$7.33^{+0.60}_{0.30}$
A 133	$1.54^{+0.10}_{-0.07}$	$10.37^{+1.27}_{-0.95}$	$0.147^{+0.012}_{-0.006}$	$1.93^{+0.58}_{-0.20}$	$0.61^{+0.06}_{-0.16}$	$1.18^{+0.35}_{-0.20}$	$0.08^{+0.01}_{-0.01}$	$7.33^{+0.65}_{-0.90}$
AWM 7	$1.52^{+0.02}_{-0.05}$	$11.5^{+0.30}_{-0.72}$	$0.150^{+0.004}_{-0.002}$	$3.60^{+0.13}_{-0.23}$	$0.78^{+0.02}_{-0.02}$	$4.16^{+0.14}_{-0.12}$	$0.09^{+0.01}_{-0.01}$	$9.65^{+0.10}_{-0.07}$
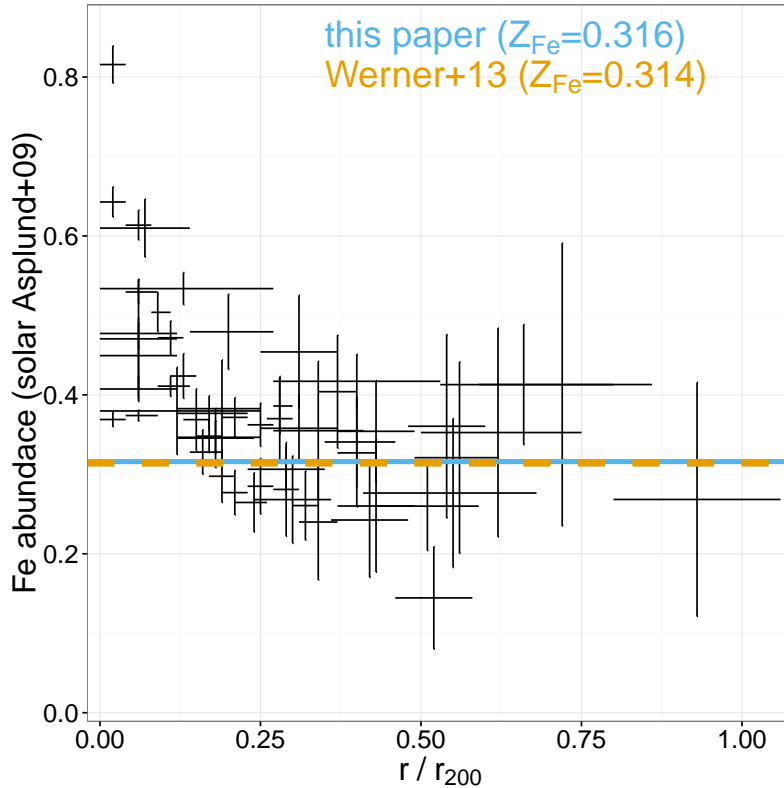
Figure 1. Iron abundance measurements in our cluster sample plotted as a function of radius scaled to r_{200}. On average, the iron abundances peak in the cores of the clusters and decrease as a function of radius, flattening at radii $r > 0.25r_{200}$. The average metallicity is shown as blue solid line. The dashed line shows the best fit metallicity reported by Werner et al. (2013) for the Perseus cluster.

moved the measurements immediately outside $0.25r_{200}$ from the subsequent analysis.

3　RESULTS

The best fit normalizations, temperatures and metallicities for the individual clusters are shown in the bottom panels of Figures A1–A9. Most of the systems in our sample are so-called cooling core clusters with bright, relatively cool, metal-rich cores. To the iron abundance measurements in this work, we also added the iron abundances measured for the non-cool core Coma cluster by Simionescu et al. (2013).

Fig. 1 shows all metallicity measurements in our cluster sample plotted as a function of radius scaled to r_{200}. The average metallicity (shown with the solid blue line) peaks in the central region and decreases as a function of radius, flattening at radii $r > 0.25r_{200}$. We tested our results for biases associated with possible multi-temperature structure by fitting the data both in the full spectral band and above 2 keV. At radii $r > 0.25r_{200}$ the two fits
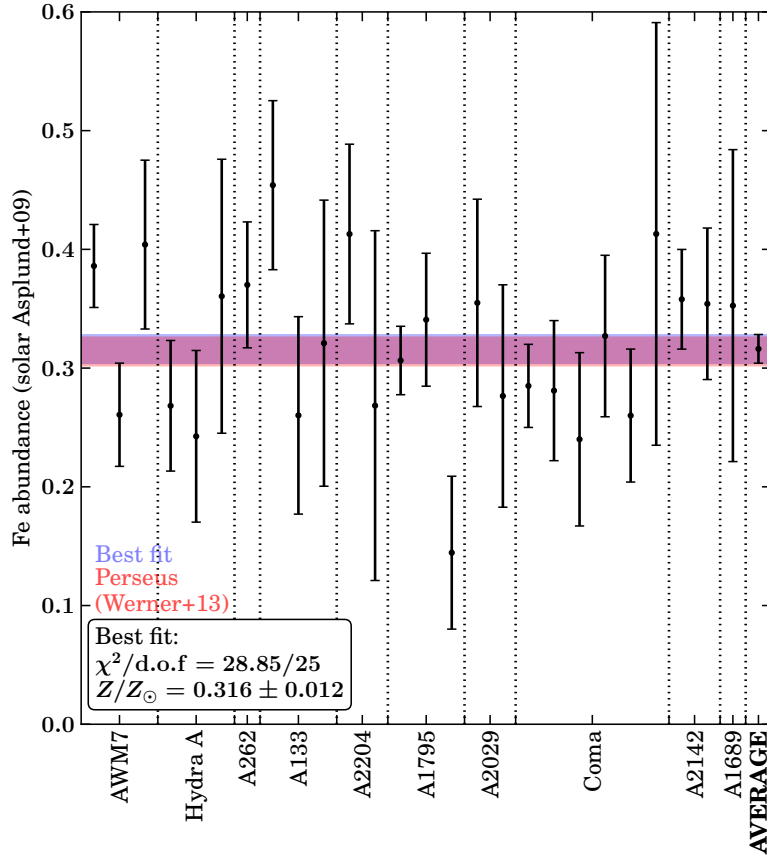
Figure 2. Robust measurements (see text for details) of the iron abundances at $r > 0.25r_{200}$ in the individual clusters. The clusters have been ordered by mass from the least to the most massive. The blue stripe marks the 68% confidence interval around the constant fit to these data, $Z_{Fe} = 0.316 \pm 0.012$ Solar. The red stripe shows the confidence interval around the best fit iron abundance reported by Werner et al. (2013) for the Perseus cluster, $Z_{Fe} = 0.314 \pm 0.012$ Solar.

provided consistent results, indicating that cooler temperature components do not contribute significantly to the observed emission in the cluster outskirts.

After excluding the measurements at $r < 0.25r_{200}$ and using all criteria outlined in the previous section, we are left with 26 individual metallicity measurements from 10 different clusters. These measurements are shown in Table 2.6 and Fig. 2 where the clusters have been ordered by mass from the least to the most massive. There is no evidence for any trend in metallicity as a function of cluster mass. The measurements are consistent with being constant at $Z_{Fe} = 0.316 \pm 0.012$ Solar, with $\chi^2 = 28.85$ for 25 degrees of freedom. This best fit value is statistically consistent with $Z_{Fe} = 0.314 \pm 0.012$ Solar reported for the Perseus cluster (Werner et al. 2013), shown as a dashed line in Fig. 1.

4   DISCUSSION

We find that across our sample of 10 clusters of galaxies the Fe abundances measured outside the central regions ($r > 0.25r_{200}$) are consistent with a constant value, $Z = 0.316 \pm 0.012$ Solar (Fig. 1). The metallicity measurements also show no significant trend with temperature (Fig. 2).

Based on the uniform iron abundance distribution in the Perseus cluster, both as a function of radius and azimuth, statistically consistent with a constant value of $Z_{Fe} = 0.314 \pm 0.012$ Solar

out to r_{200}, Werner et al. (2013) proposed that most of the metal enrichment of the intergalactic medium occurred before clusters formed, probably more than ten billion years ago ($z > 2$), during the period of maximal star formation and black hole activity. A key prediction of the early enrichment scenario is that the ICM in all massive clusters should be uniformly enriched to a similar level. Previous indications for a uniform ICM enrichment include the small cluster to cluster scatter in the Fe abundance observed within r_{500} (Matsushita 2011; Leccardi & Molendi 2008) and the observed pre-enrichment of the ICM between the clusters Abell 399/401 (Fujita et al. 2008). Our observation of a constant iron abundance at large radii across a sample of 26 independent measurements for ten massive clusters further confirms this early enrichment scenario. This early enrichment could have been driven by galactic winds (De Young 1978) which would be strongest around the peak of star formation and AGN activity (redshifts $z \sim 2 - 3$ Madau et al. 1996; Brandt & Hasinger 2005).

Recent numerical simulations by Fabjan et al. (2010) and Biffi et al. (2017) indicate that while star-formation and supernova feedback are unable to enrich the intergalactic medium uniformly, simulations which also include feedback from AGN produce remarkably homogeneous metallicity distribution in the ICM out to large radii. They show that the uniform metallicity is the result of a widespread displacement of metal-rich gas by powerful AGN outbursts that occure *before* the epoch of maximal star-formation and AGN activity. Biffi et al. (2017) conclude that early AGN feedback acting on high-

Table 5. Measurement radii and the best fit metallicities measured in our cluster sample.

cluster	r/r_{200}	$Z/Z_{\odot}$
	0.285 ± 0.015	0.386 ± 0.035
AWM7	0.32 ± 0.02	0.261 ± 0.043
	0.37 ± 0.03	0.404 ± 0.071
	0.30 ± 0.06	0.268 ± 0.055
Hydra A	0.42 ± 0.06	0.243 ± 0.072
	0.54 ± 0.06	0.361 ± 0.115
A262	0.28 ± 0.02	0.370 ± 0.053
	0.31 ± 0.06	0.454 ± 0.071
A133	0.43 ± 0.06	0.260 ± 0.083
	0.56 ± 0.07	0.321 ± 0.120
A2204	0.66 ± 0.13	0.413 ± 0.076
	0.93 ± 0.13	0.268 ± 0.147
	0.29 ± 0.06	0.306 ± 0.029
A1795	0.40 ± 0.05	0.341 ± 0.056
	0.52 ± 0.06	0.145 ± 0.064
A2029	0.34 ± 0.07	0.355 ± 0.087
	0.55 ± 0.14	0.276 ± 0.094
A2142	0.31 ± 0.06	0.358 ± 0.042
	0.43 ± 0.06	0.354 ± 0.064
A1689	0.62 ± 0.12	0.353 ± 0.131
	0.25 ± 0.02	0.285 ± 0.035
Coma[†]	0.29 ± 0.02	0.281 ± 0.059
	0.34 ± 0.03	0.240 ± 0.072
	0.40 ± 0.03	0.327 ± 0.068
	0.50 ± 0.08	0.260 ± 0.056
	0.71 ± 0.13	0.41 ± 0.18
Average metallicity		0.316 ± 0.012

[†]Simionescu et al. (2013)

redshift ($z > 2$) small haloes, with shallow gravitational potential wells, was particularly efficient in spreading and mixing the metals. Given the complexity of the physics of the chemical enrichment processes, these simulation results should probably be considered tentative. However, our measurements provide an important anchor with which the results of these and future simulations can be compared, bringing more understanding into the process of chemical enrichment.

The constant ratios of abundances of several elements observed throughout the Virgo cluster (Simionescu et al. 2015) as well as in the radial profiles of 44 clusters observed out to intermediate radii with *XMM-Newton* (Mernier et al. 2017) reveal that, during the early period of metal enrichment, the products of core-collapse and type Ia supernovae were well mixed. The estimated ratio between the number of SN Ia and the total number of supernovae enriching the ICM is about 15–20%, generally consistent with the metal abundance patterns in our own Galaxy and only marginally lower than the SN Ia contribution estimated for the cluster cores (Simionescu et al. 2015).

The most direct way to confirm the early enrichment scenario is to measure the core-excluded metallicity of clusters as a function of redshift. Contrary to initial findings (Balestra et al. 2007; Maughan et al. 2008; Anderson et al. 2009; Baldi et al. 2012), under the early enrichment scenario, there should be no substantial redshift evolution in the ICM metallicity outside the central regions of clusters, out to $z \sim 2$. Recent results (Andreon 2012; Ettori et al. 2015; McDonald et al. 2016; Mantz et al. 2017) indicate that most metals in the ICM were already in place at $z = 1$, consistent with the picture of an early enrichment.

At various overdensities, the chemical enrichment might pro-

ceed on different time scales or with different initial mass functions, resulting in a trend with cluster mass. Within the mass range probed by our sample (factor of ~ 10), there is no evidence for dependence of ICM metallicity on total cluster mass. A more thorough analysis of the mass dependence will require reliable measurements of absolute abundances in low mass clusters and groups of galaxies, which are often made difficult for current CCD instruments by multi-temperature structure in the ICM (Simionescu et al. 2015, 2017). A lack of trend with cluster mass would either indicate a rate of metal enrichment in the early Universe that is independent of the density contrast between different regions, or a very high efficiency of mixing on large scales.

If the ICM at large radii is clumpy and multiphase (Simionescu et al. 2011; Urban et al. 2014; Simionescu et al. 2017) then its best fit metallicity, derived using a single temperature model, might be biased (Avestruz et al. 2014). The best fit Fe abundance is the most significantly biased at temperatures around 1 keV, where its value is determined based on the Fe-L lines, which are very sensitive to the underlying temperature structure (see Buote 2000). The metallicities of the clusters in our sample are determined using the Fe-K lines and depending on the temperature structure could be biased by at most 30 per cent (both toward higher and lower values; Rasia et al. 2008; Simionescu et al. 2009; Gastaldello et al. 2010). The fact that the spectral fits in the full band and above 2 keV give consistent results (see Section 3) indicates that if substantially cooler, denser clumps are present in the ICM, they do not contribute significantly to the observed emission measure and the metal budget.

In the near future, the metallicities of groups and cooler clusters could be further studied with the *Astrosat* satellite (Singh et al. 2014). The low earth orbit and the small inclination of the orbital plane of *Astrosat* provide a low and stable background environment that is required for cluster outskirts studies. The large field of view provides a sufficient grasp, enabling mapping the faint X-ray emission in the outskirts of nearby clusters that span large angular scales in the sky. Such observations will further test the possible mass-dependence of metallicity. Deep observations with *XMM-Newton* and *Chandra* will allow us to precisely determine the metallicity outside the cores of high redshift clusters, providing further constraints on the redshift evolution of metallicity. Observations with high spectral resolution obtained with the *X-ray Astronomy Recovery Mission (XARM)* will allow more accurately measured relative abundance ratios for clusters at low redshifts, testing our models of nucleosynthesis. In the further future, missions like *Athena* (Nandra et al. 2013) or *Lynx*[7] will allow detailed studies of metal abundances in high redshift clusters, providing comprehensive understanding of the metal cycle in the Universe.

5 CONCLUSIONS

Here, we report 26 independent metallicity measurements in the outskirts ($r > 0.25r_{200}$) of ten nearby galaxy clusters. These measurements are consistent with a constant value $Z_{\rm Fe} = 0.316 \pm 0.012$ Solar. No significant trend of metallicity versus temperature or mass is observed.

Our results corroborate the conclusions drawn from previous metallicity measurements at large radii in the Perseus cluster (Werner et al. 2013). In particular, they confirm the predictions of

[7] https://wwwastro.msfc.nasa.gov/lynx/

an early enrichment scenario, where the majority of metal enrichment occurs before the cluster formation, at $z > 2$.

REFERENCES

Akamatsu H., Hoshino A., Ishisaki Y., et al., 2011, PASJ, 63, 1019

Anderson M. E., Bregman J. N., Butler S. C., Mullis C. R., 2009, ApJ, 698, 317

Andreon S., 2012, A&A, 546, A6

Arnaud K. A., 1996, in Astronomical Data Analysis Software and Systems V, edited by G. H. Jacoby, J. Barnes, vol. 101 of Astronomical Society of the Pacific Conference Series, 17

Arnaud M., Pointecouteau E., Pratt G. W., 2005, A&A, 441, 893

Asplund M., Grevesse N., Sauval A. J., Scott P., 2009, *Ann. Rev. Astr. Astrophys.*, 47, 481

Avestruz C., Lau E. T., Nagai D., Vikhlinin A., 2014, ApJ, 791, 117

Baldi A., Ettori S., Molendi S., Balestra I., Gastaldello F., Tozzi P., 2012, A&A, 537, A142

Balestra I., Tozzi P., Ettori S., et al., 2007, A&A, 462, 429

Bautz M. W., Miller E. D., Sanders J. S., et al., 2009, PASJ, 61, 1117

Biffi V., Planelles S., Borgani S., et al., 2017, [arXiv:1701.08164]

Böhringer H., Werner N., 2010, AAPR, 18, 127

Brandt W. N., Hasinger G., 2005, *Ann. Rev. Astr. Astrophys.*, 43, 827

Buote D. A., 2000, MNRAS, 311, 176

Cash W., 1979, ApJ, 228, 939

De Grandi S., Ettori S., Longhetti M., Molendi S., 2004, A&A, 419, 7

De Luca A., Molendi S., 2004, A&A, 419, 837

de Plaa J., Werner N., Bleeker J. A. M., Vink J., Kaastra J. S., Méndez M., 2007, A&A, 465, 345

De Young D. S., 1978, ApJ, 223, 47

Ettori S., Baldi A., Balestra I., Gastaldello F., Molendi S., Tozzi P., 2015, A&A, 578, A46

Fabjan D., Borgani S., Tornatore L., Saro A., Murante G., Dolag K., 2010, MNRAS, 401, 1670

Fujimoto R., Mitsuda K., Mccammon D., et al., 2007, PASJ, 59, 133

Fujita Y., Tawa N., Hayashida K., et al., 2008, PASJ, 60, 343

Gastaldello F., Ettori S., Balestra I., et al., 2010, A&A, 522, A34

Giodini S., Pierini D., Finoguenov A., et al., 2009, ApJ, 703, 982

Ikebe Y., Reiprich T. H., Böhringer H., Tanaka Y., Kitayama T., 2002, A&A, 383, 773

Ishisaki Y., Maeda Y., Fujimoto R., et al., 2007, PASJ, 59, 113

Kalberla P. M. W., Burton W. B., Hartmann D., et al., 2005, A&A, 440, 775

Kuntz K. D., Snowden S. L., 2000, ApJ, 543, 195

Lacey C., Cole S., 1993, MNRAS, 262, 627

Leccardi A., Molendi S., 2008, A&A, 486, 359

Madau P., Ferguson H. C., Dickinson M. E., Giavalisco M., Steidel C. C., Fruchter A., 1996, MNRAS, 283, 1388

Mantz A. B., Allen S. W., Morris R. G., et al., 2017, MNRAS submitted, [arXiv: 1706.01476]

Masui K., Mitsuda K., Yamasaki N. Y., et al., 2009, PASJ, 61, 115

Matsushita K., 2011, A&A, 527, A134

Maughan B. J., Jones C., Forman W., Van Speybroeck L., 2008, ApJS, 174, 117

McDonald M., Bulbul E., de Haan T., et al., 2016, ApJ, 826, 124

Mernier F., de Plaa J., Kaastra J. S., et al., 2017, [arXiv: 1703.01183]

Mernier F., de Plaa J., Pinto C., et al., 2016, A&A, 595, A126

Morandi A., Cui W., 2014, MNRAS, 437, 1909

Mushotzky R. F., Holt S. S., Boldt E. A., Serlemitsos P. J., Smith B. W., 1981, ApJ, 244, L47

Mushotzky R. F., Serlemitsos P. J., Boldt E. A., Holt S. S., Smith B. W., 1978, ApJ, 225, 21

Nandra K., Barret D., Barcons X., et al., 2013, [arXiv: 1306.2307]

Neill J. D., Brodie J. P., Craig W. W., Hailey C. J., Misch A. A., 2001, ApJ, 548, 550

Piffaretti R., Arnaud M., Pratt G. W., Pointecouteau E., Melin J.-B., 2011, A&A, 534, A109

Rasia E., Mazzotta P., Bourdin H., et al., 2008, ApJ, 674, 728

Reiprich T. H., Hudson D. S., Zhang Y.-Y., et al., 2009, A&A, 501, 899

Sato T., Sasaki T., Matsushita K., et al., 2012, PASJ, 64, 95

Sidher S. D., Sumner T. J., Quenby J. J., Gambhir M., 1996, A&A, 305, 308

Simionescu A., Allen S. W., Mantz A., et al., 2011, Science, 331, 1576

Simionescu A., Werner N., Böhringer H., et al., 2009, A&A, 493, 409

Simionescu A., Werner N., Mantz A., Allen S. W., Urban O., 2017, MNRAS, 469, 1476

Simionescu A., Werner N., Urban O., et al., 2013, ApJ, 775, 4

Simionescu A., Werner N., Urban O., Allen S. W., Ichinohe Y., Zhuravleva I., 2015, ApJ, 811, L25

Singh K. P., Tandon S. N., Agrawal P. C., et al., 2014, in Space Telescopes and Instrumentation 2014: Ultraviolet to Gamma Ray, vol. 9144 of *Proc. SPIE*, 91441S

Smith R. K., Brickhouse N. S., Liedahl D. A., Raymond J. C., 2001, ApJ, 556, L91

Umetsu K., Broadhurst T., 2008, ApJ, 684, 177

Urban O., Simionescu A., Werner N., et al., 2014, MNRAS, 437, 3939

Voges W., Aschenbach B., Boller T., et al., 1999, A&A, 349, 389

Walker S. A., Fabian A. C., Russell H. R., Sanders J. S., 2014, MNRAS, 442, 2809

Walker S. A., Fabian A. C., Sanders J. S., George M. R., Tawara Y., 2012, MNRAS, 422, 3503

Werner N., Durret F., Ohashi T., Schindler S., Wiersma R. P. C., 2008, *Space Sci. Rev*, 134, 337

Werner N., Urban O., Simionescu A., Allen S. W., 2013, Nature, 502, 656

Yoshino T., Mitsuda K., Yamasaki N. Y., et al., 2009, PASJ, 61, 805

APPENDIX A: INDIVIDUAL CLUSTERS
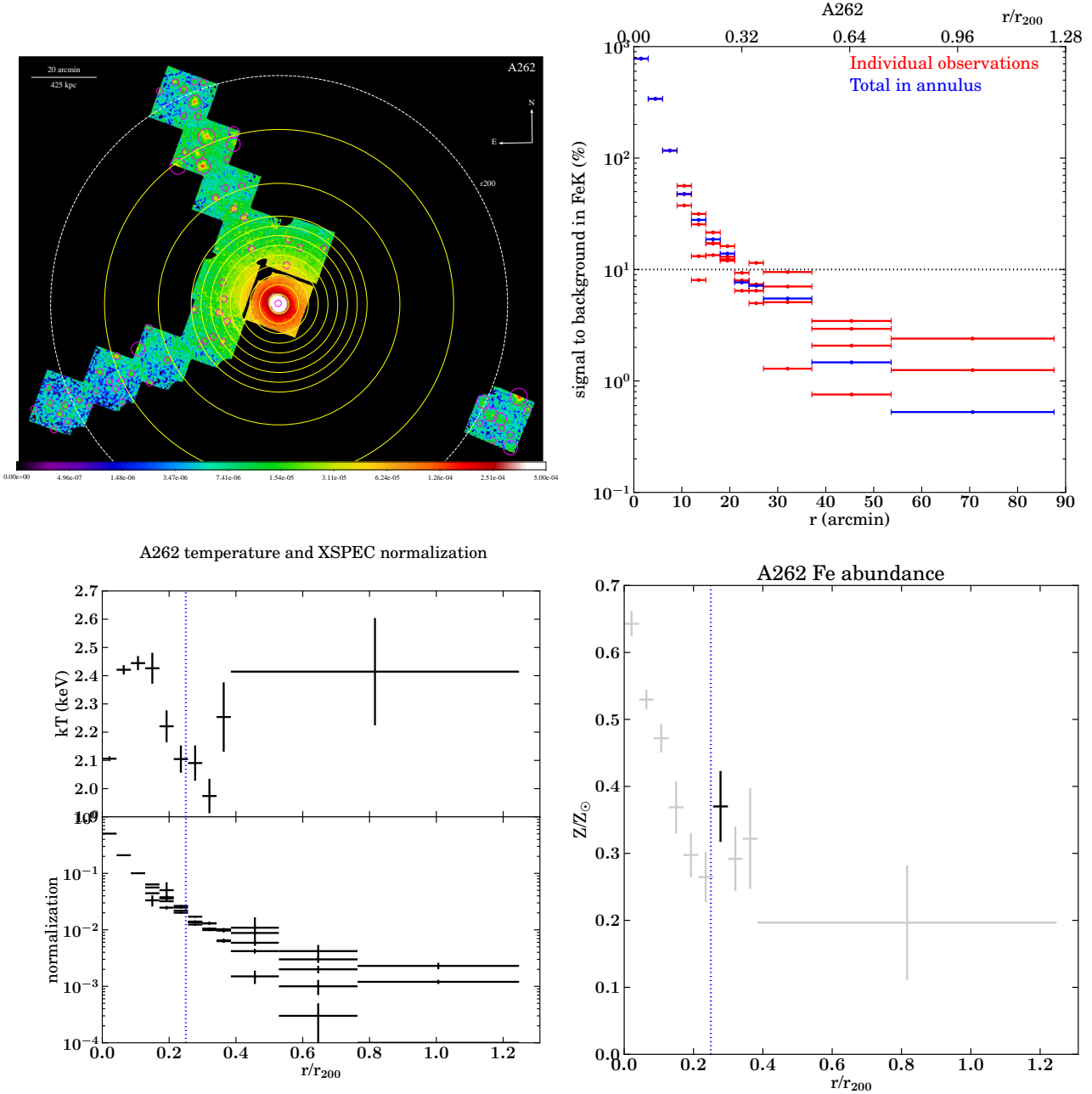
Figure A1. *Top left:* The exposure- and vignetting corrected mosaic of the *Suzaku* observations of A 262 in the $0.7 - 7.0$ keV energy range. The image has been smoothed with a Gaussian with width of 25 arcsec. The dashed white circle has a radius of r_{200}. Small magenta circles show the point sources removed from the spectral analysis. The annular regions, within which we measured the ICM metallicity, are shown in yellow. The colour bar shows the surface brightness in units of counts s^{-1} arcmin^{-2}. *Top right:* Ratio of the number of the ICM counts to the sum of CXFB and the instrumental background counts in a 1 keV-wide energy band around the Fe-K line, in the individual observations (*red*) and for the complete annulus (*blue*). The dotted line marks the 10% threshold employed for all subsequent analysis. For observations where the ratio is close to zero, the data point does not appear in the plot. *Bottom left:* Projected temperature and normalisation profiles of A262 (the units of the normalisation are defined in Tab. 4). The horizontal axes shows the distance from the cluster center in the units of r_{200} shown in Tab. 2. The vertical dotted line marks $0.25r_{200}$, which we conservatively assume to be the outside border of the central metallicity peak. *Bottom right:* Radial profile of the best fit projected iron abundance. Only the black data points were included in our subsequent analysis.
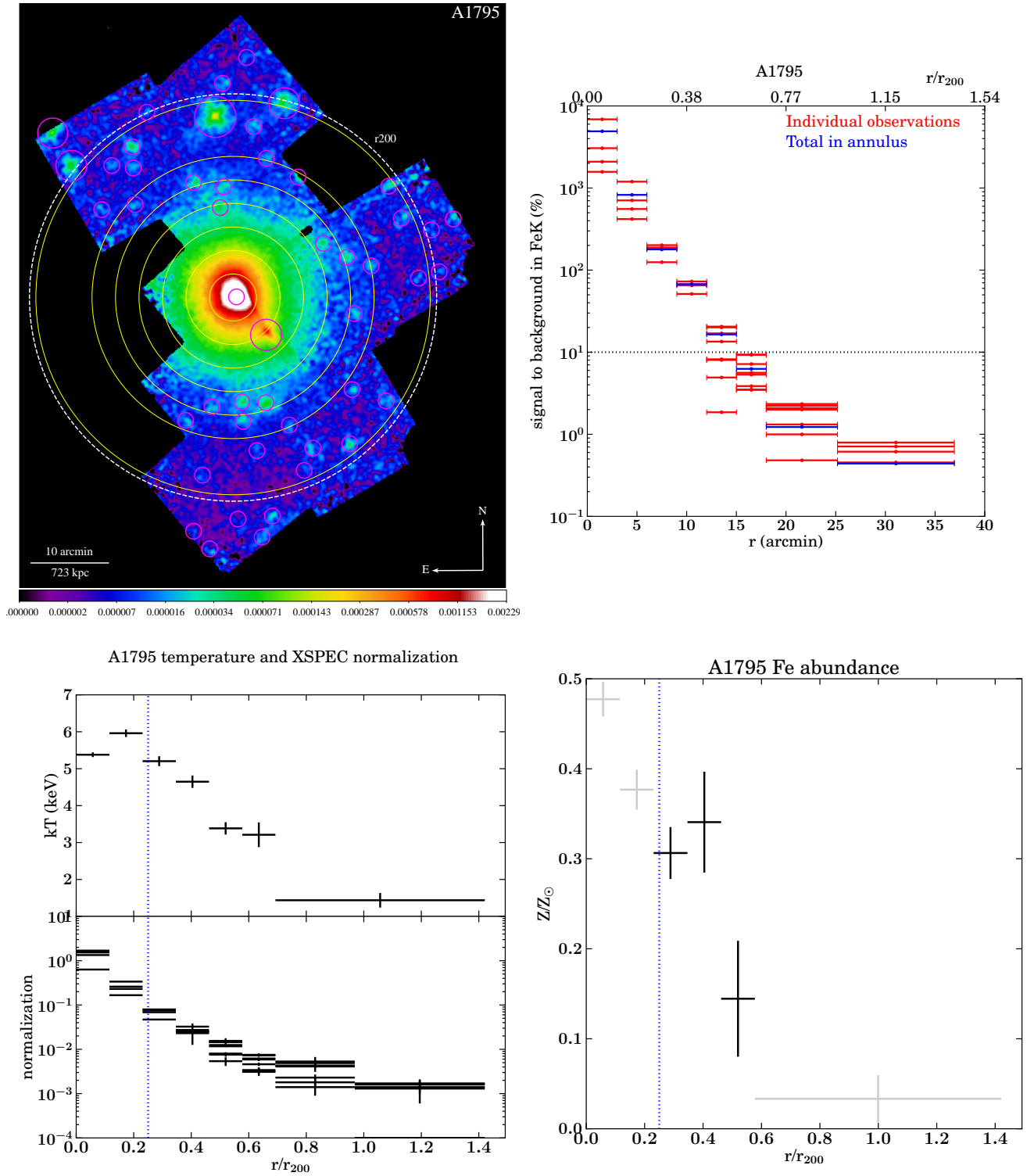
Figure A2. Same as Fig. A1, but for A 1795.
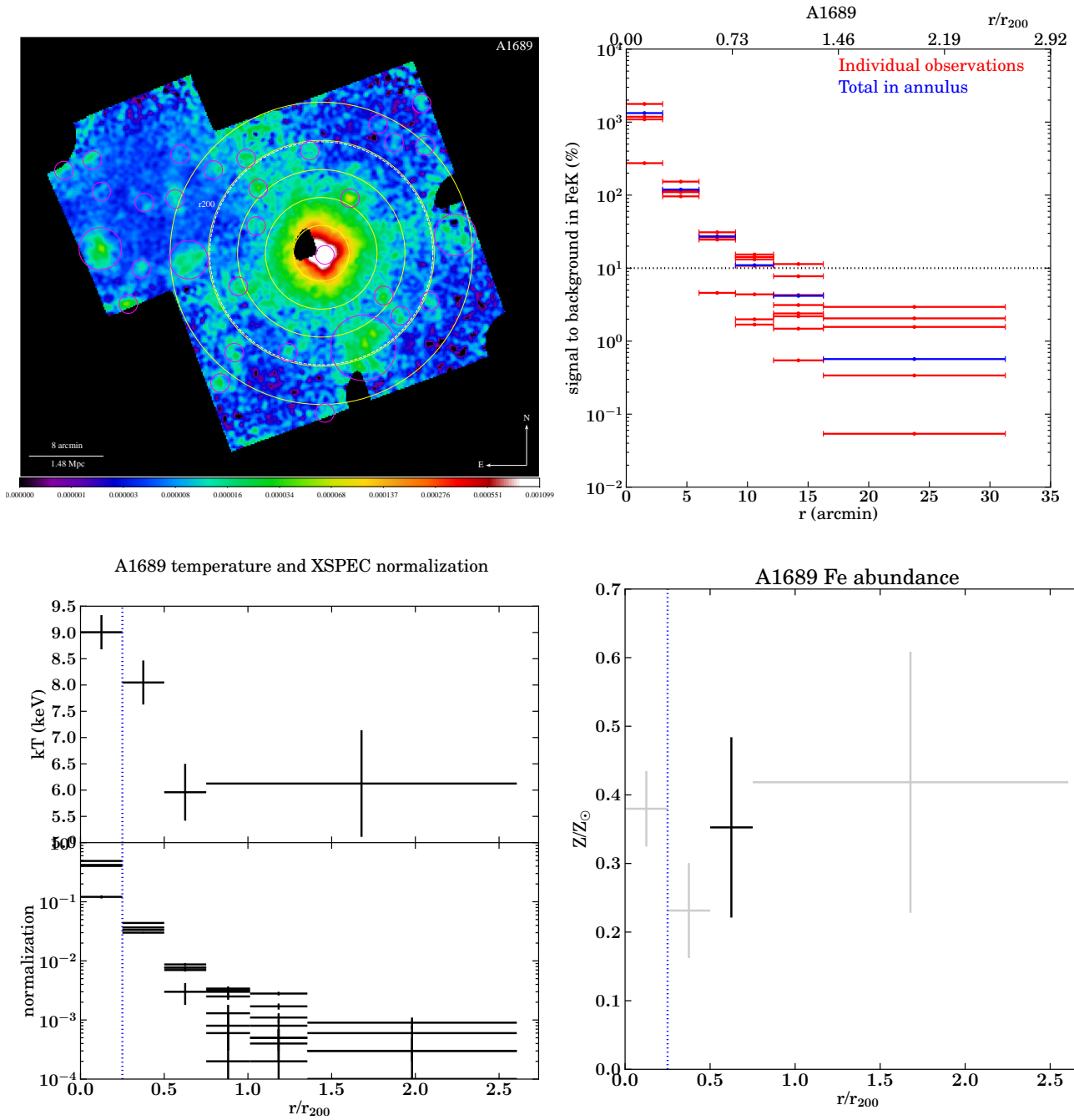
Figure A3. Same as Fig. A1, but for A 1689.
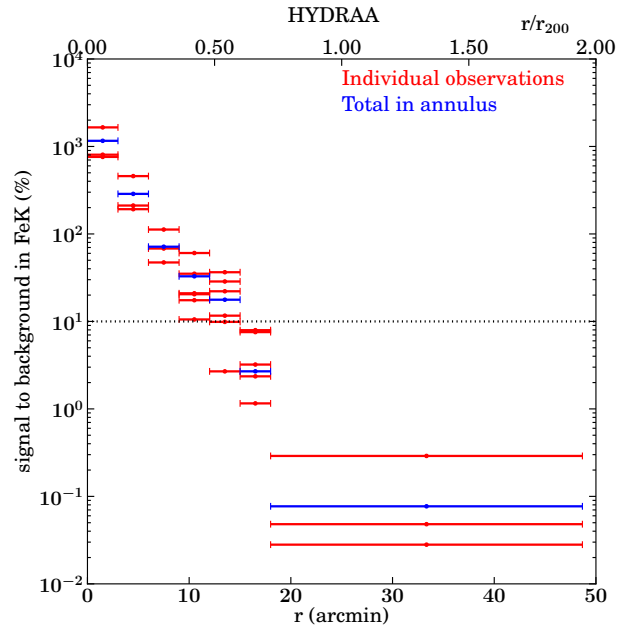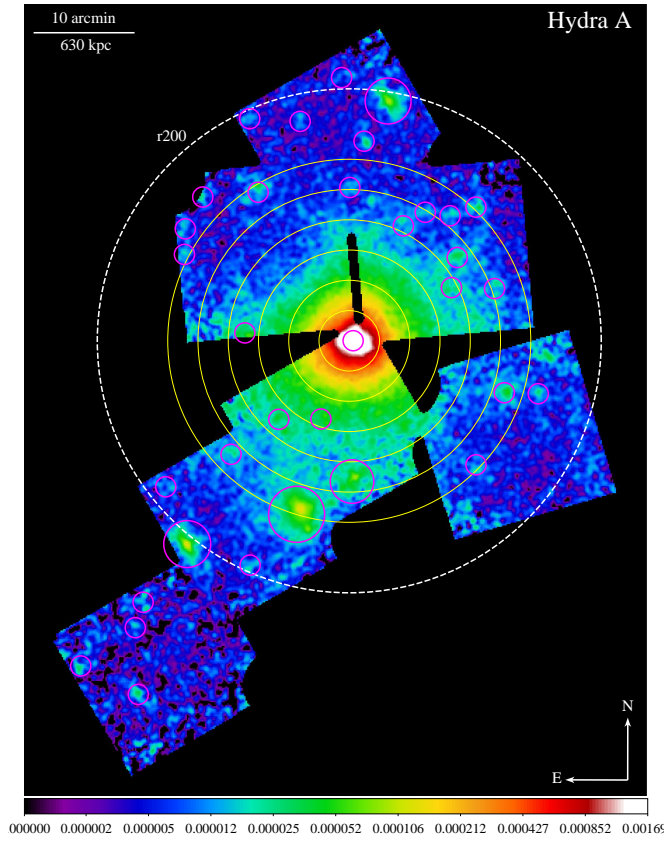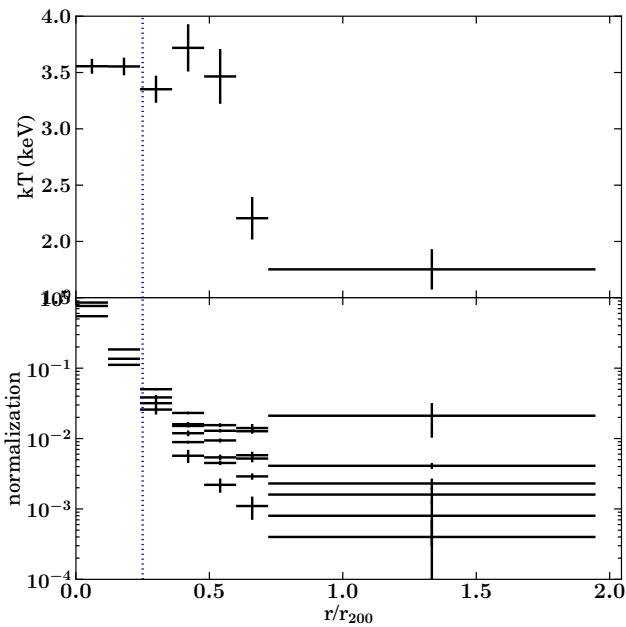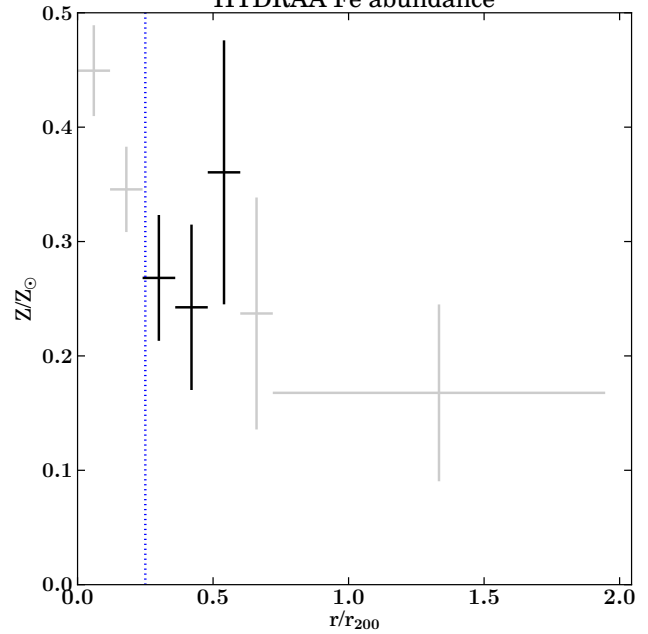
Figure A4. Same as Fig. A1, but for Hydra A.
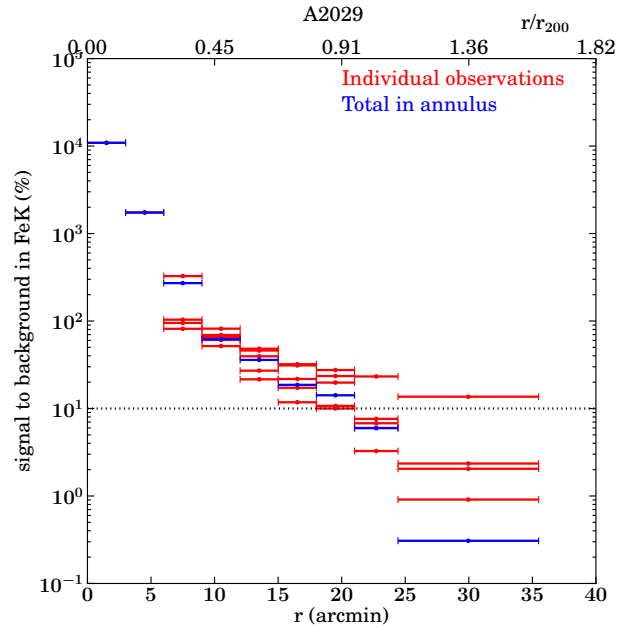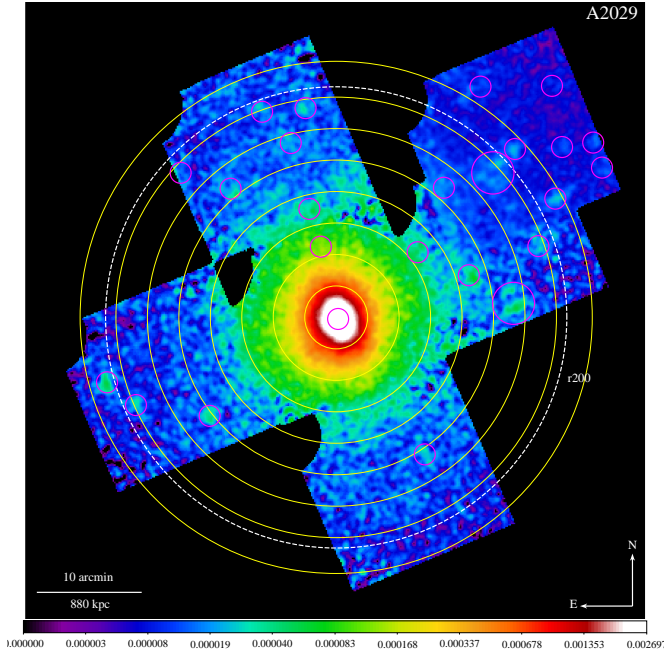
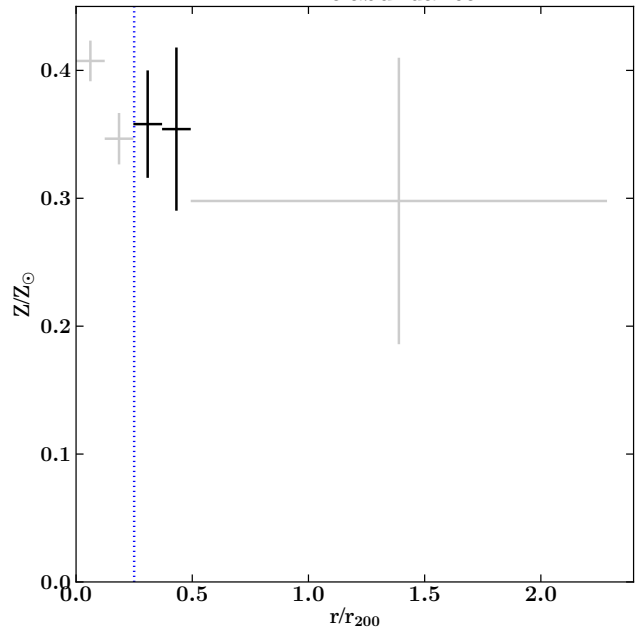**Figure A5.** Same as Fig. A1, but for A 2029.
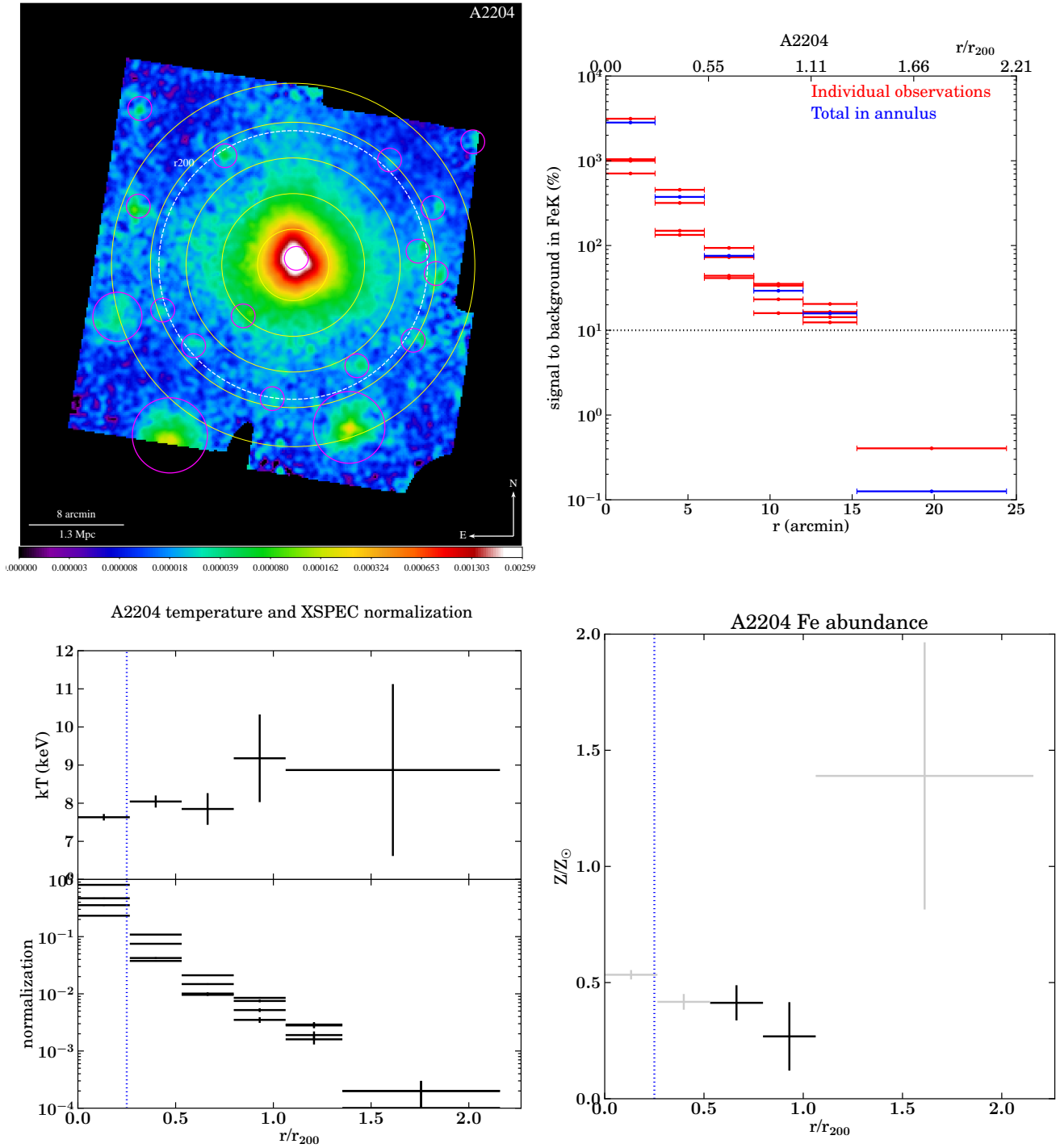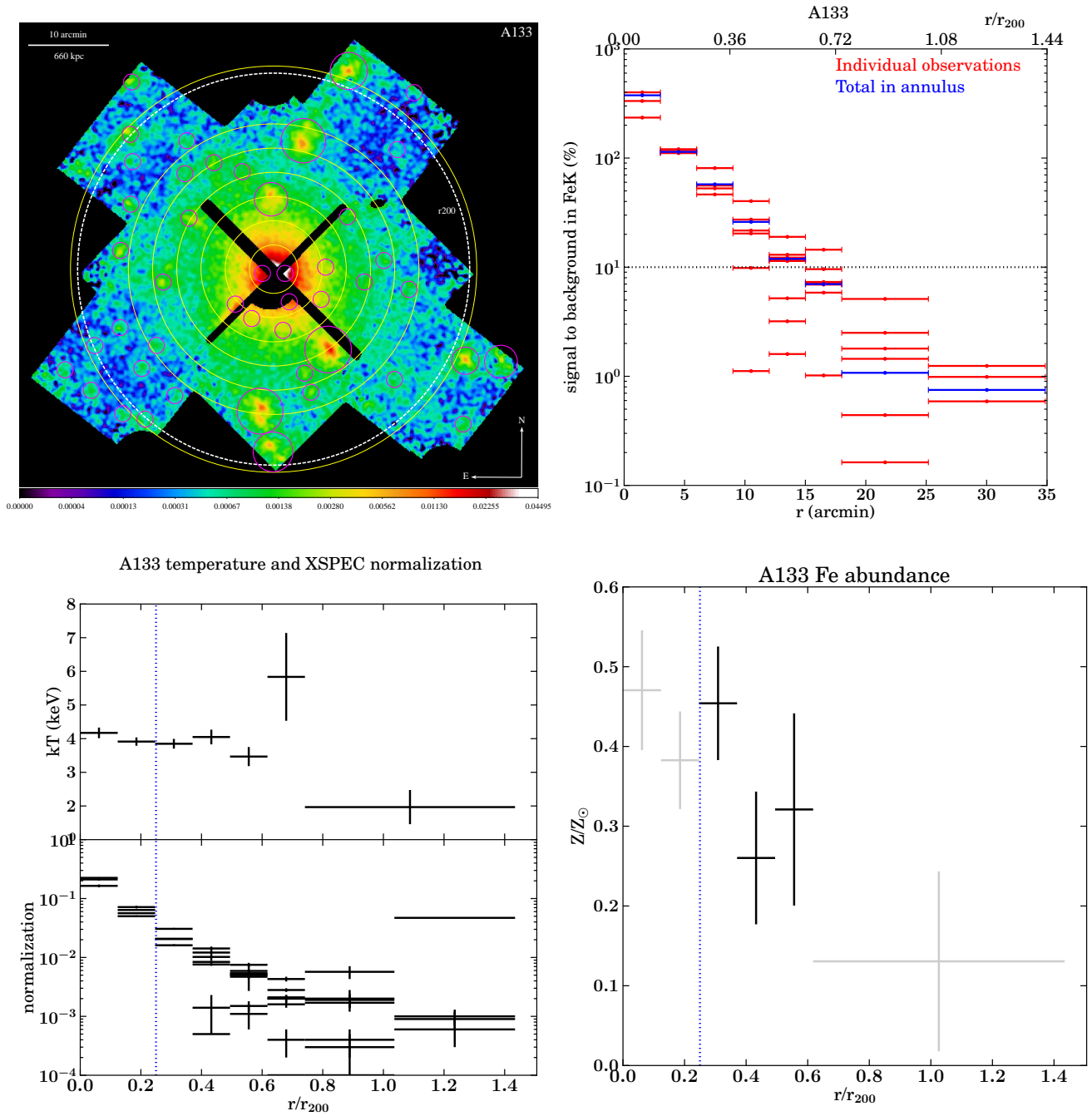
Figure A6. Same as Fig. A1, but for A 2204.
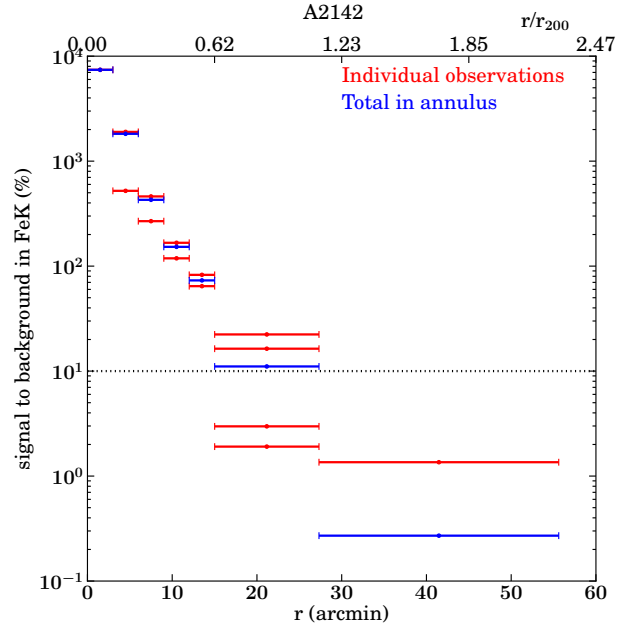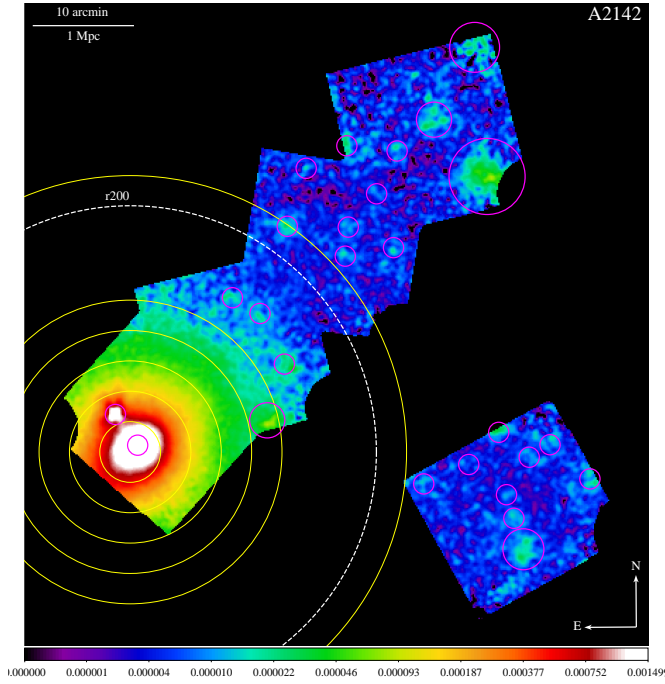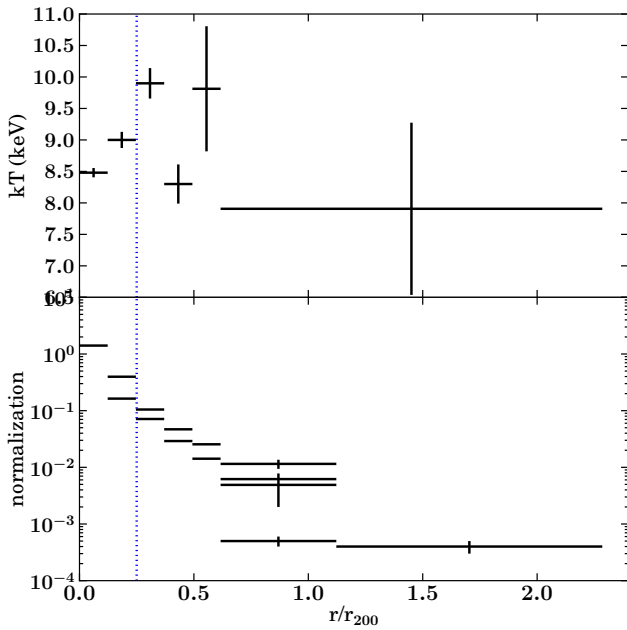
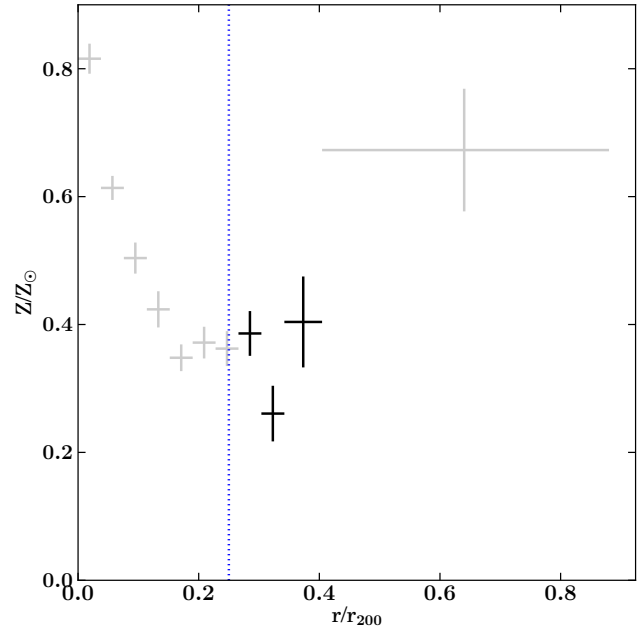**Figure A7.** Same as Fig. A1, but for A 2142.

Figure A8. Same as Fig. A1, but for A 133.
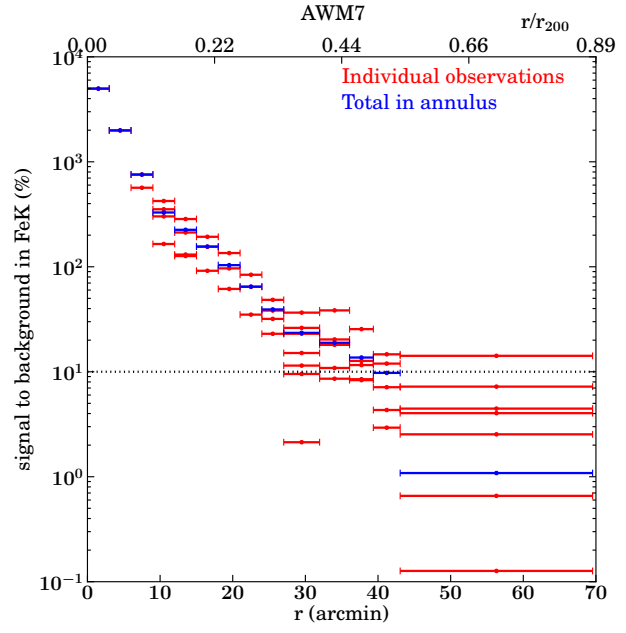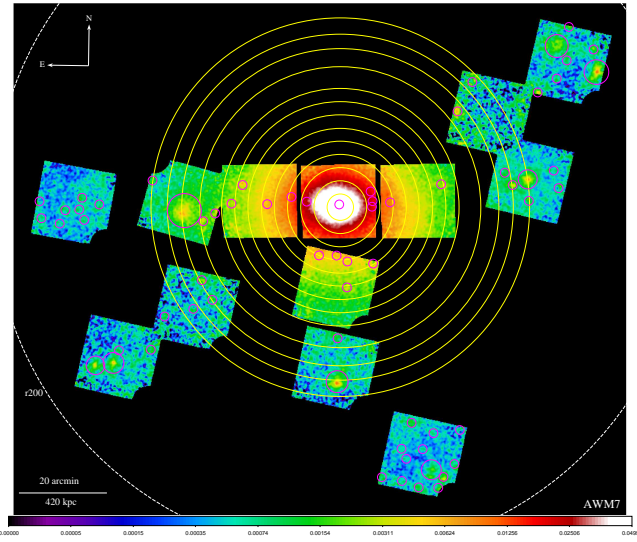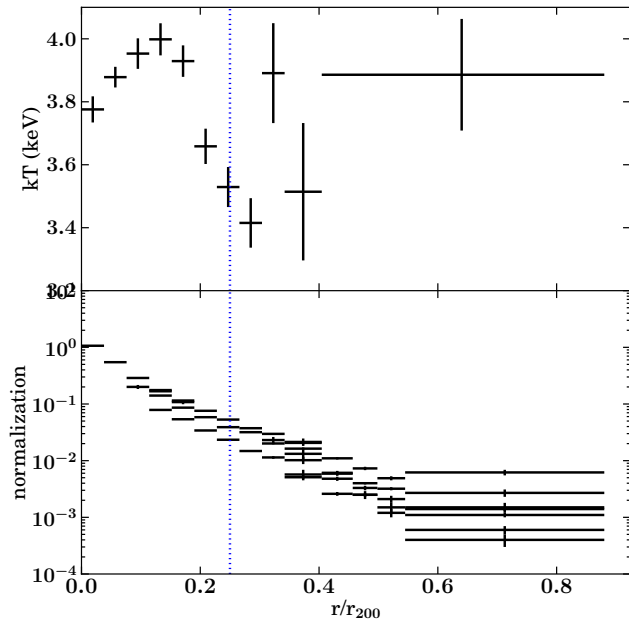
Figure A9. Same as Fig. A1, but for AWM7.